Geophysical Research Letters

RESEARCH LETTER
10.1029/2019GL086601

Two Dimensional Full-Wave Modeling of Propagation of Low-Altitude Hiss in the Ionosphere

Xiang Xu[1,2], Chen Zhou[1], Lunjin Chen[2], Zhiyang Xia[2], Xu Liu[2], Jamesina J. Simpson[3], and Yuannong Zhang[1]

[1]Department of Space Physics, School of Electronic Information, Wuhan University, Wuhan, China, [2]William B. Hanson Center for Space Sciences, University of Texas at Dallas, Richardson, TX, USA, [3]Department of Electrical and Computer Engineering, University of Utah, Salt Lake City, UT, USA

Key Points:
- Mode conversion from whistler to H^+ band EMIC and polarization reversal occur simultaneously where wave frequency matches H^+–He^+ crossover frequency
- The wave normal angle dependence of mode conversion efficiency determines the features of low-altitude hiss observed by low orbit satellite in the ionosphere
- Low-altitude hiss emission of whistler mode can be converted to left-hand polarized EMIC with efficiency maximized with wave normal angle near 45°

Supporting Information:
- Supporting Information S1

Correspondence to:
C. Zhou and L. Chen,
chenzhou@whu.edu.cn;
lunjin.chen@gmail.com

Citation:
Xu, X., Zhou, C., Chen, L., Xia, Z., Liu, X., Simpson, J. J., & Zhang, Y. (2020). Two dimensional full-wave modeling of propagation of low-altitude hiss in the ionosphere. *Geophysical Research Letters*, *47*, e2019GL086601. https://doi.org/10.1029/2019GL086601

Received 18 DEC 2019
Accepted 27 JAN 2020
Accepted article online 18 FEB 2020

Abstract We investigate the propagation characteristics of low-altitude hiss in the ionosphere by numerical simulation with a two-dimensional full-wave model. The simulation results demonstrate that linear mode conversion from whistler to H^+ band electromagnetic ion cyclotron wave and polarization reversal occur simultaneously where wave frequency matches the H^+–He^+ crossover frequency. This mode conversion efficiency shows sensitive dependence on wave normal angle and plays a significant role in the propagation of whistler emission near the local proton gyro-frequency in the ionosphere by redistributing the wave energy below and above the H^+–He^+ cutoff frequency, which can explain the low-altitude hiss observed by the Freja and Detection of Electromagnetic Emissions Transmitted from Earthquake Regions satellites, respectively. The energy of whistler-mode low-altitude hiss emission can be transferred to reflected left-hand polarized electromagnetic ion cyclotron through mode conversion and the efficiency reaches a maximum for intermediate incident wave normal angle (of 45°).

1. Introduction

Plasmaspheric hiss is usually observed inside the high-density plasmasphere in the extremely low frequency range from ~100 Hz to ~2 kHz. Plasmaspheric hiss is generally known as naturally occurring broadband incoherent whistler mode emission (Dunckel & Helliwell, 1969; Russell et al., 1969; Thorne et al., 1973), which is of vital importance in the formation of the structure of radiation belt (Abel & Thorne, 1998; Lyons & Thorne, 1973). Ray tracing studies have suggested that chorus emission outside the plasmapause can propagate into the plasmasphere at high latitude, confined inside the plasmasphere due to magnetospheric reflection or steep gradient of plasmapause and evolve into plasmaspheric hiss (Chum & Santolík, 2005; Bortnik et al., 2008; Bortnik et al., 2011; Chen et al., 2012). This mechanism of chorus being embryonic source of plasmaspheric hiss has later been supported by satellite observations (Bortnik et al., 2009; Li et al., 2015).

Reflection due to the plasmapause not only contributes to the formation of plasmaspheric hiss but also enables a portion of plasmaspheric hiss to propagate out of the plasmasphere and access the high latitude ionosphere as low-altitude hiss, which has been confirmed by ray tracing simulation (Chen et al., 2017; Santolík et al., 2006). A subsequent conjugative observation of low-altitude hiss in the ionosphere from DEMETER (Detection of Electromagnetic Emissions Transmitted from Earthquake Regions) and plasmaspheric hiss from Time History of Events and Macroscale Interactions during Substorms provides further evidence that low-altitude hiss can be an ionospheric manifestation of plasmaspheric hiss (Zhima et al., 2017).

Propagation characteristics of low-altitude hiss in the ionosphere over a typical frequency range of ~100 Hz to ~ 1 kHz have been investigated with low orbit satellite observations from Freja and DEMETER (Chen et al., 2017; Santolík et al., 2006; Santolík & Parrot, 1998, 1999, 2000; Xia et al., 2019). The ionospheric hiss emission is categorized by the propagation characteristics in existing literature. Different names may be given because of different satellite data used. Both type C emission from Freja (Figures 3 and 4 of Santolík & Parrot, 1999) and type I emission from DEMETER (Figure 1 of Chen et al., 2017) manifest a wide frequency range at high latitude and propagate downward along the ambient magnetic field line with right-hand circular polarization. Different from the type C and type I emissions, types A and F emissions from Freja (Figures 3 and 4 of Santolík & Parrot, 1999) and type II emission from DEMETER (Figure 1 of Chen

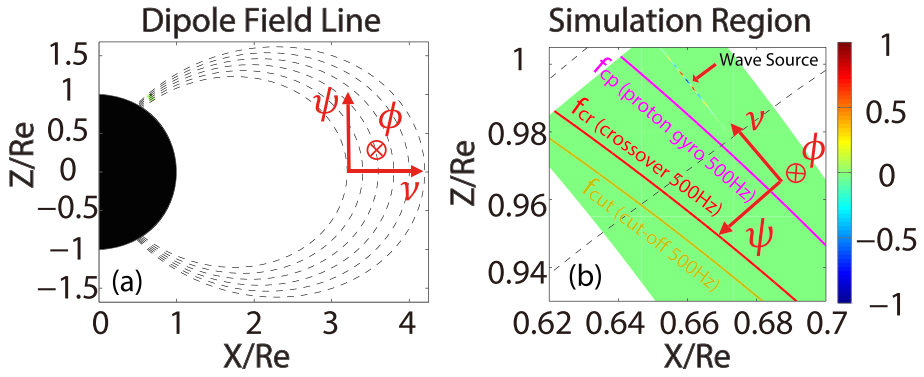

Figure 1. (a) Scheme of the structure of the dipole field used in our simulation system. The green filled area at high latitude denotes the simulation region. (b) Normalized power of the spatially varying Gaussian wave source at t = 0 s. The dashed curves are dipole field lines. The magenta, red, and golden lines denote where the wave frequency matches the local proton gyro-frequency f_{cp}, the local H^+–He^+ crossover frequency f_{cr} and the H^+–He^+ cutoff frequency f_{cut}. The ψ, ν and ϕ axis are shown in both panels.

et al., 2017; Figure 1 of Xia et al., 2019) show a sharp cutoff near the local proton gyro-frequency. Type A emission is downward propagating while type F emission is upward propagating. Both types of emissions propagate toward lower latitude with highly oblique wave normal angle (WNA) and right-hand elliptical polarization (Santolík & Parrot, 1999). Type II emission is observed at lower latitudes with a narrow range of frequency and a mixture of right-hand, left-hand, and linear polarization and propagates toward equator (Chen et al., 2017).

A recent ray tracing study shows that types I and II emissions are connected and both originate from whistler-mode plasmaspheric hiss and explains the equatorward propagation of type II emission with the wave trapping mechanism due to the H^+–He^+ cutoff frequency and the negatively radial gradient of the ionospheric plasma density near the local proton gyro-frequency (Chen et al., 2017; Xia et al., 2019). Although ray tracing method has been widely used in the investigation of the propagation of plasma waves in the ionosphere and the magnetosphere, it is generally limited to the situations where Wentzel-Kramers-Brillouin approximation is satisfied and mode coupling is not considered. However, during the propagation of low-altitude hiss below the local proton gyro-frequency in the ionosphere, Wentzel-Kramers-Brillouin approximation may become invalid and the possibility of mode coupling is significantly increased because of the large gradient of plasma density and geomagnetic field, so a new method such as full-wave modeling is necessary in our investigation to properly address the problem of propagation including possible mode coupling (Budden, 1985; Chust & Le Que´au, 1996; Stix, 1992). In this study, we perform a two-dimensional full-wave simulation to investigate the propagation characteristics of low-altitude hiss to account for various observation characteristics mentioned above. The paper is organized as follows: We introduce the two dimensional full-wave model used in our simulation in section 2. In section 3, we show the simulation results and finally conclusion and discussion come in section 4.

2. Full Wave Model

2.1. Basic Equations

We model the propagation of low-altitude hiss emission as the extension of whistler wave near the local proton gyro-frequency in a dipolar magnetic field, under the assumption that the low-altitude hiss originates from magnetospheric whistler mode waves (Chen et al., 2017; Xia et al., 2019; Zhima et al., 2017). The following electromagnetic wave equations based on cold plasma theory are numerically solved (Helliwell, 1965; Stix, 1992):

$$\frac{\partial \mathbf{H}}{\partial t} = -\frac{1}{\mu_0}\nabla\times\mathbf{E} \tag{1}$$

$$\frac{\partial \mathbf{J}_\alpha}{\partial t} + \nu_\alpha \mathbf{J}_\alpha = \varepsilon_0 \omega_{p\alpha}^2 \mathbf{E} - \boldsymbol{\omega}_{c\alpha}\times\mathbf{J}_\alpha \tag{2}$$

$$\mathbf{J}_e = \nabla\times\mathbf{H} - \sum_\alpha \mathbf{J}_\alpha \tag{3}$$

$$\mathbf{E} = \frac{\nu_e}{\varepsilon_0\omega_{pe}^2}\mathbf{J}_e - \frac{\mathbf{J}_e\times\boldsymbol{\omega}_{ce}}{\varepsilon_0\omega_{pe}^2} \tag{4}$$

Equation (1) is Ampere's law and equation (2) is the linearized momentum equation for ion species denoted by α, including H^+, He^+, and O^+ in our study. Equation (3) is Faraday's law with displacement current neglected because of the low frequency approximation (Hu & Denton, 2009; Streltsov et al., 2006). Equation (4) is the linearized momentum equation for electrons with inertial term eliminated because the wave frequency of interest is much lower than the lower hybrid resonance frequency. μ_0 and ε_0 are vacuum permeability and permittivity, respectively. ν_α and ν_e are collision frequency for α ion species and electron, respectively. $\omega_{p\alpha}$ and ω_{pe} are plasma frequency for α ion species and electron, respectively. $\boldsymbol{\omega}_{c\alpha}$ and $\boldsymbol{\omega}_{ce}$ are gyro-frequency for α ion species and electron, respectively. $\mathbf{E}$ and $\mathbf{H}$ are electric and magnetic field, respectively. $\mathbf{J}_\alpha$ and $\mathbf{J}_e$ are plasma currents due to the velocity oscillation of α ion species and electron, respectively, under the assumption that the density perturbation is a higher order effect on the currents in the linear limit.

2.2. Coordinate System

A modified dipole coordinate system (ψ,ν,ϕ) (Kageyama et al., 2006) is adopted to solve the full wave equations and it is defined by spherical coordinates (r,θ,ϕ) with

$$\psi = \frac{sinh^{-1}\left(\frac{a\cos\theta}{r^2}\right)}{sinh^{-1}a} \tag{5}$$

$$\nu = \frac{\sin^2\theta}{r} \tag{6}$$

As illustrated in Figure 1a, the ψ axis is directed along the ambient magnetic field, the ν axis is in the meridian plane and perpendicular to the ψ axis, and the ϕ axis is along azimuthal direction. The parameter a in equation (5) is used to adjust the spatial grid of ψ axis in the simulation region. The realistic grid spacing along ψ axis changes rapidly in a standard dipole coordinate from the equator to high latitude, causing an unnecessarily severe numerical stability constraint. With the proper setting of the parameter a of an empirical value ~100, the realistic grid spacing varies slowly in the modified dipole coordinate system without significantly affecting the simulation results. The simulation system is in the meridian plane and we only consider propagation of whistler emission in ψ direction and ν direction.

2.3. Numerical Technique

Finite-Difference Time-Domain method is used to solve the equation (1) (Liu et al., 2018; Taflove & Hagness, 2005; Yee, 1966) to update $\mathbf{H}$ field. $\mathbf{J}_\alpha$ field due to α ion species is updated by solving the equation (2) with a modified Boris method (suitable for both collisionless and collisional regimes) following Samimi and Simpson (2015).

2.4. Boundary Condition

An absorbing condition is used in the simulation system (Streltsov et al., 2012) by setting the collision frequency ν_α to zero in the simulation region (reasonable at topside ionosphere (Gurevich, 1978; Schunk & Nagy, 2000)) and enhancing it quadratically close to the boundaries. This leads to rapid damping of wave energy in the boundary layers so no significant wave energy can reflect back to the simulation region. The absorbing boundary condition is used for both upper and lower ψ and ν boundaries.

2.5. Simulation Setup

In our two-dimensional full wave simulation, a magnetic dipole field

$$\boldsymbol{B}_0 = \frac{\nabla\psi}{|\nabla\psi|}B_{eq}\left(\frac{1}{Lcos^2\theta}\right)^3\sqrt{1+3sin^2\theta} \tag{7}$$

is adopted as the ambient magnetic field, where $\frac{\nabla\psi}{|\nabla\psi|}$ is the unit vector along ψ axis, B_{eq} is the equatorial magnetic field strength, L is L-shell value, and θ is the magnetic latitude. A diffusive equilibrium plasma density

model (Bortnik et al., 2011) is adopted as plasma density profile including H^+, He^+, O^+, and electrons. The parameter values of the density model used in this paper are the same as in Bortnik et al. (2011).

A spatially varying Gaussian wave source along ν axis is set up for H_ϕ component, which oscillates sinusoidally at wave frequency f (above the local proton gyro-frequency) with a certain initial WNA. Along this line source, H_ϕ component adopts the form

$$H_\phi(\nu,t) = sin\left(\int k_\nu h_\nu d\nu + 2\pi f t\right) exp\left(-\frac{(L-L_0)^2}{D_L^2}\right) \tag{8}$$

where L_0 and D_L are the center and half width of the spatial Gaussian distribution of the wave source, respectively. $h_\nu = \frac{1}{|\nabla\nu|}$ is the metric term defined in the coordinate system. The perpendicular wave number k_ν is obtained from the cold plasma dispersion of the whistler mode for given WNA and f at the central location of the line source, to ensure that the source wave propagates at the chosen WNA. A localized absorbing region is set right above the wave source to damp the wave propagating upward from the source so that we only focus on the incident wave propagating downward. Wave source and characteristic frequencies (local proton gyro-frequency f_{cp}, H^+–He^+ crossover frequency f_{cr} and H^+–He^+ cutoff frequency f_{cut}) in the simulation region are introduced in Figure 1. The definition and equations for the crossover and cutoff frequencies may be found in equations (A1)–(A6) in Appendix A in Chen et al. (2014).

During the simulation, the **E**, **H,** and **J** vectors in each computational cell of the simulation system are sampled in the time domain. Using these sampled signals, we can obtain the following wave properties: The time averaged Poynting vector calculated with

$$\boldsymbol{S} = \frac{1}{T}\int \mathbf{E}\times\mathbf{H}dt \tag{9}$$

where T is the whistler wave period; the polar angle of the Poynting vector calculated using the components of $\boldsymbol{S}$; The WNA and ellipticity of the magnetic field polarization calculated by the Means (1972) method; the kinetic energy density calculated with

$$W_k = \frac{1}{T}\int \sum_\alpha \frac{m_\alpha}{2e^2 N_\alpha}\left(J_\psi^2 + J_\nu^2 + J_\phi^2\right)dt \tag{10}$$

where m_α is the mass of electron and ions, N_α is the plasma density, and e is the elementary charge.

3. Simulation Results

First, we simulate the propagation of whistler emissions with an intermediate initial WNA just above f_{cp}. The wave frequency is 500 Hz and the initial WNA is 42°. The wave source is centered at the location of $L = 3.90$, magnetic latitude 56.42° and altitude 0.19 R_e and the half width D_L is 0.078. The L-shell range of the simulation region is from 3.16 to 4.10, and the magnetic latitude range is from 52° to 58°. The simulation is run over 400 wave periods, after which the wave intensity distribution reaches a nearly steady state and does not vary significantly. The simulation results are presented in Figure 2. Damped waves in collisional absorbing region are not shown in this paper.

The incident whistler emission from above f_{cp} splits near f_{cut} into one portion tunneled to lower altitude and the other portion reflecting upward. The standing wave pattern (Figure 2a) and the enhancement of the normalized kinetic energy density (Figure 2c) both indicate that the reflection occurs between f_{cr} and f_{cut}. The reflected wave also splits with one portion below f_{cp} and the other propagating to higher altitude, as indicated by the interference wave pattern (Figure 2a) and the normalized wave intensity (represented by Poynting flux magnitude normalized by the maximum magnitude in Figure 2b). The intensity of the reflected wave below f_{cp} is higher than both the reflected portion above f_{cp} and the tunneled wave below f_{cut} by 1 order of magnitude (Figure 2b). Moreover, the kinetic energy density of the reflected wave below f_{cp} is significantly higher than the other portion (Figure 2c). The ellipticity of magnetic field polarization (Figure 2d) shows that the incident wave above f_{cr}, the tunneled wave below f_{cut} and the reflected wave

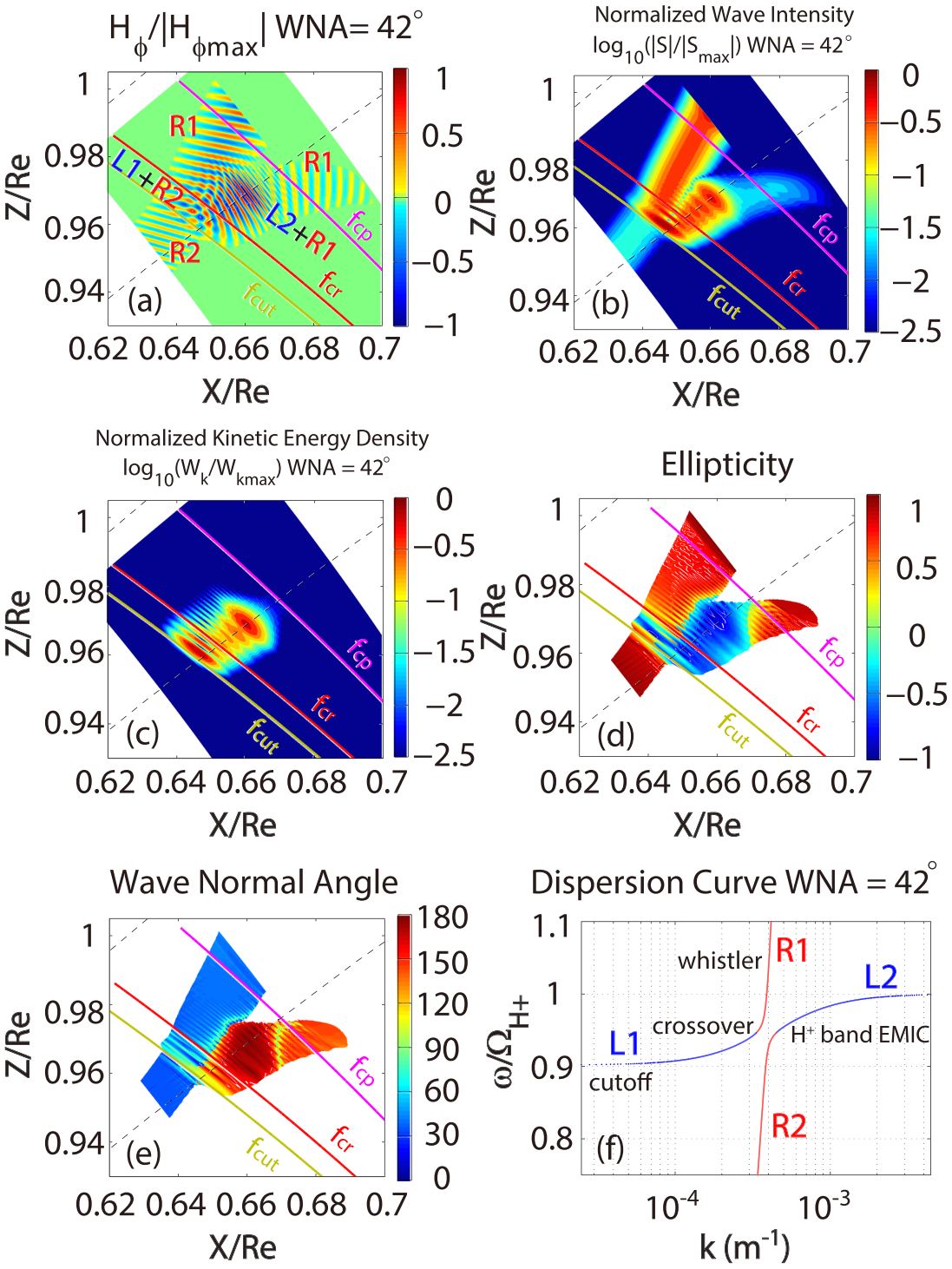

Figure 2. Simulation results from whistler propagation with an initial WNA of 42° near f_{cp} and the dispersion curves for this case. (a) H_ϕ component with a normalized amplitude $\frac{H_\phi}{|H_{\phi max}|}$. (b) Normalized wave intensity $log_{10}\left(\frac{|S|}{|S_{max}|}\right)$. (c) Normalized kinetic energy density $log_{10}\left(\frac{W_k}{W_{kmax}}\right)$. (d) Ellipticity of magnetic field polarization. "1" (−1) is for purely right-hand (left-hand) circular polarization and "0" is for linear polarization. (e) WNA with respect to the ambient magnetic field. "0" (180) denotes wave normal parallel (antiparallel) to the ambient magnetic field. (f) Dispersion curves. The horizontal axis is the wave number and the vertical axis is the wave frequency normalized to the local proton gyro-frequency Ω_{H^+}. Two different branches, whistler and H^+ band EMIC, are shown and labeled accordingly. The red (blue) curve denotes the right-hand (left-hand) polarization. The right-hand (left-hand) polarized whistler is labeled as R1 (L1). The right-hand (left-hand) polarized H^+ band EMIC is labeled as R2 (L2).

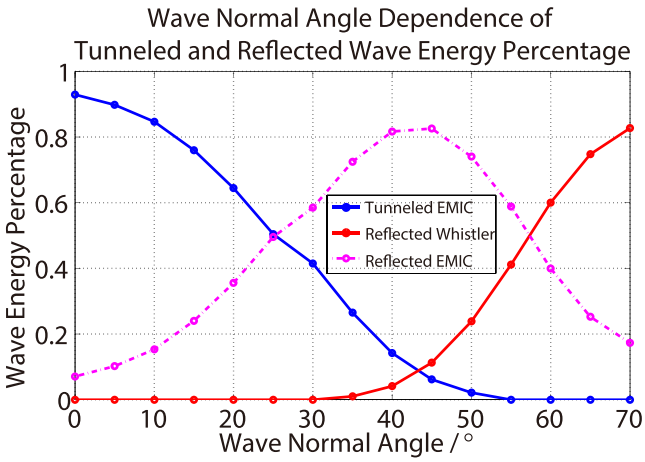

Figure 3. WNA dependence of tunneled and reflected wave energy percentage. The horizontal axis is the initial WNA of the incident whistler above f_{cp}. The vertical axis is the wave energy percentage. The blue solid and magenta dash-dotted lines denote the wave energy percentage of tunneled EMIC wave and reflected EMIC wave generated from mode coupling, respectively. The red solid line denotes the wave percentage of reflected whistler wave above f_{cp}.

above f_{cp} are all right-hand polarized. However, the reflected wave between f_{cr} and f_{cp} is left-hand polarized. Moreover, a mixture of linear and left-hand polarization is shown between f_{cr} and f_{cut}. Figure 2e shows the WNA. Interestingly, the reflected wave is oblique below f_{cr} and above f_{cp} while nearly parallel to the ambient magnetic field between f_{cr} and f_{cp}. Figure 2f shows the dispersion curves for whistler with WNA of 42°, propagating near f_{cr}. The ratio $\frac{\omega_{pe}}{\omega_{ce}} = 0.76$ and the ion composition is 10.51% H^+, 87.02% O^+, and 2.47% He^+. Two dispersion branches (Figure 2f), whistler and H^+ band electromagnetic ion cyclotron (EMIC), are separated from each other. For a medium of uniform plasma density and magnetic field, the incident whistler emission from above f_{cp} would propagate down along the whistler branch and reflect at f_{cut}. However, large inhomogeneity of the plasma density and rapid change of ion composition in the ionosphere lead to the coupling of the two wave modes at f_{cr} (Budden, 1985; Chust & Le Que´au, 1996; Stix, 1992). With the dispersion curves and the simulation results shown in Figure 2, we can explain the propagation characteristics of whistler emission with intermediate WNA near f_{cp}. Right-hand polarized incident whistler emission from above f_{cp} (R1 in Figure 2) splits at f_{cr}. One portion is converted to a right-hand polarized H^+ band EMIC (R2) through linear mode coupling and is tunneled down below f_{cr} and further below f_{cut}. The other portion undergoes polarization reversal, propagates with left-hand polarization (L1), and reflects upward at f_{cut}. The left-hand polarized reflected wave (L1) splits again at f_{cr}. One portion experiences a second polarization reversal, changing from left-hand polarized (L1) to right-hand polarized whistler (R1) while the other portion is converted to a left-hand polarized H^+ band EMIC (L2) through mode conversion at f_{cr}. The propagation of the H^+ band EMIC wave with left-hand polarization (L2) is nearly parallel to the ambient magnetic field, and the wavelength is becoming shorter when wave frequency approaches f_{cp} (Figures 2a and 2e). Since the left-hand polarized EMIC wave cannot propagate beyond f_{cp}, the kinetic energy and wave intensity accumulates near f_{cp} (Figure 2b and 2c) due to the decreasing group velocity.

To quantify the distribution of wave energy among different modes, we define the tunneled wave energy percentage and reflected wave energy percentage using the following equations:

$$\eta_{tunnel} = \frac{\int |\boldsymbol{S}_{tunR2}| h_\nu d\nu}{\int |\boldsymbol{S}_{incR1}| h_\nu d\nu} \tag{11}$$

$$\eta_{reflect} = \frac{\int |\boldsymbol{S}_{refR1}| h_\nu d\nu}{\int |\boldsymbol{S}_{incR1}| h_\nu d\nu} \tag{12}$$

$|\boldsymbol{S}_{tunR2}|$ is the wave intensity of the right-hand polarized tunneled EMIC wave below f_{cut} (R2), $|\boldsymbol{S}_{incR1}|$ ($|\boldsymbol{S}_{refR1}|$) is the wave intensity of incident (reflected) right-hand polarized whistler above f_{cp} (R1). For the above simulation shown in Figure 2, the tunneled wave energy percentage is 10% while the reflected whistler wave energy percentage is 6%. The significant discrepancy between the sum of the two percentages from unity is due to the accumulated EMIC wave energy (L2) between f_{cr} and f_{cp}.

The above simulation is repeated with initial WNA increased from 0° to 70° with step of 5° (detailed wave properties of some typical cases are shown in the supporting information), and the results of wave energy percentage are shown in Figure 3. The tunneled EMIC wave energy percentage decreases with the WNA (Figure 3). In other words, the efficiency of mode conversion from whistler wave to right-hand polarized H+ band EMIC wave at f_{cr} decreases with the increase of incident WNA. The tunneled wave energy percentage is high (~80% or higher) with WNA smaller than 15°, which explains the features of type C hiss observed by Freja satellite (Santolík & Parrot, 1999) and type I hiss observed by DEMETER satellite (Chen et al., 2017) in the high-latitude ionosphere. Hiss emissions of these two types are below f_{cp} with right-hand polarization, propagating downward along the magnetic field line with small WNA (~15° or smaller). Furthermore, the

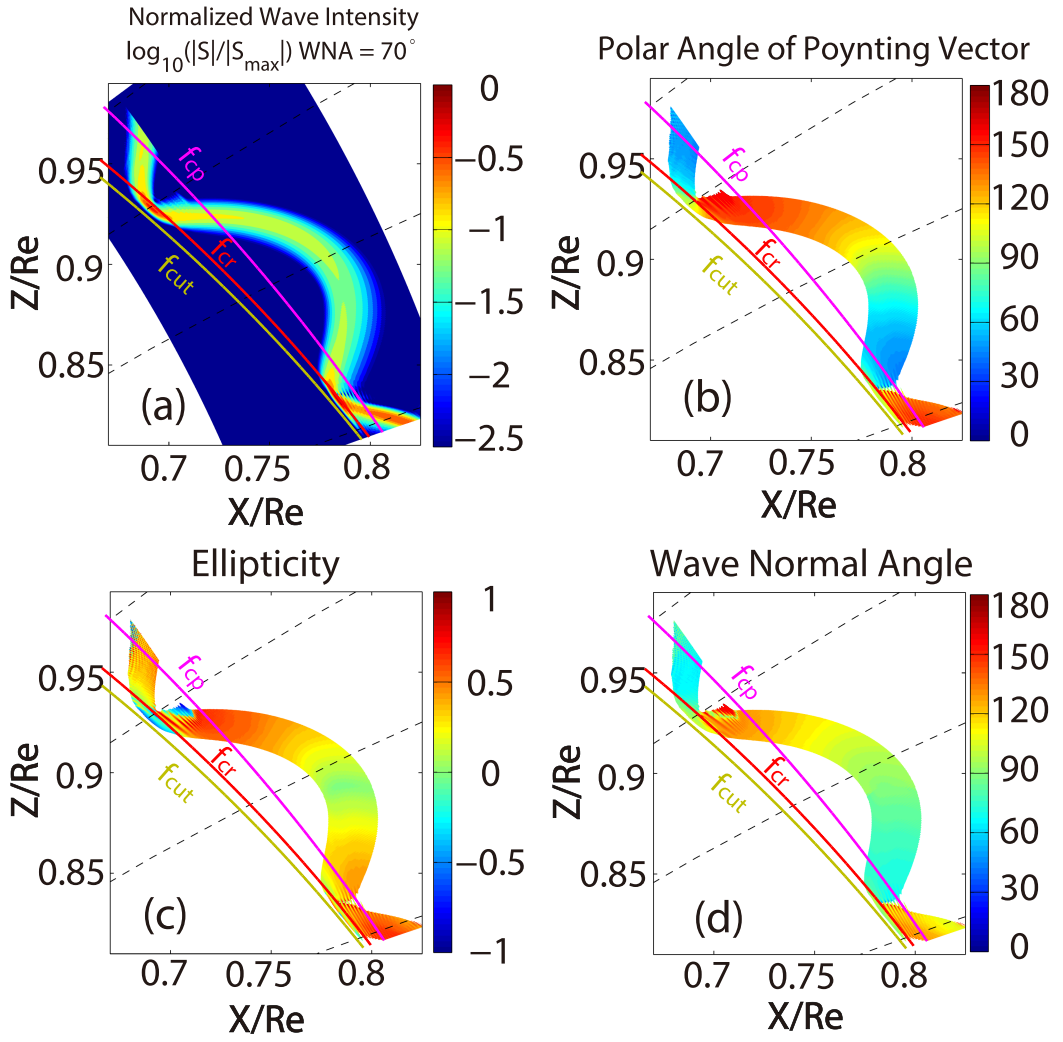

Figure 4. Simulation results from whistler propagation with initial WNA of 70° near f_{cp}. (a) Normalized wave intensity $log_{10}\left(\frac{|S|}{|S_{max}|}\right)$. (b) Polar angle of Poynting vector S with respect to the ambient magnetic field. "0" (180) represents wave energy propagation parallel (antiparallel) to the ambient magnetic field. (c) Ellipticity of magnetic field polarization. (d) WNA with respect to the ambient magnetic field.

tunneled wave energy percentage decreases to nearly zero with the critical WNA of 55°. Contrary to the tunneled wave, the reflected whistler wave energy percentage is nearly zero with WNA smaller than 30° and growing to over 80% with WNA increased to 70°. For those large initial WNAs, the mode coupling essentially vanishes. The discrepancy of the sum of the two percentages from unity (shown by magenta dash-dotted line in Figure 3) denotes the mode conversion efficiency to generate reflected upward propagating left-handed EMIC waves above f_{cr} and below f_{cp}. From Figure 3, we can see the efficiency reaches a maximum value at intermediate incident WNA (about 45°). Finally, we present the simulation of whistler mode propagation with large initial WNA of 70°, at which the mode coupling essentially vanishes, over an extended region to verify the existence of the waveguide predicted by ray tracing analysis (Chen et al., 2017). The simulation region is extended such that the L-shell ranges from 2.32 to 3.73 and the magnetic latitude ranges from 44° to 56°. The wave source is centered at $L = 3.55$, the magnetic latitude of 54.67° and the altitude of 0.19 R_e, and the half width D_L is 0.126. The simulation is run over 700 wave periods, after which the wave intensity distribution reaches a nearly steady state and does not vary significantly. The simulation results are presented in Figure 4. These results demonstrate that most of the right-hand polarized incident whistler energy is transferred to the right-hand polarized upward propagating whistler emission after the reflection near f_{cut}. No significant wave energy is

tunneled below f_{cut} and the left-hand polarized reflected EMIC wave intensity is much weaker compared to the case with an initial WNA of 42°. As shown in Figure 4, whistler emission with an incident WNA of 70° from high latitude propagates in an oscillatory path, trapped in the vicinity of f_{cp} and guided toward the Equator, which is consistent with the recent ray tracing study (Chen et al., 2017). These simulation results also explain the propagation of types A and F hiss observed by the Freja satellite (Santolík & Parrot, 1999) and type II hiss observed by the DEMETER satellite (Chen et al., 2017; Xia et al., 2019) at lower latitude. These types of hiss emissions propagate equatorward with a large WNA over 65° with a sharp frequency cutoff near f_{cp}. Moreover, the upgoing propagation and left-hand polarization of these hiss emissions near f_{cut} can be explained by the reflection of whistler emission from f_{cut} and the polarization reversal at f_{cr} respectively (Figures 4b–4d).

4. Conclusions and Discussion

The propagation of low-altitude hiss in the ionosphere is studied by numerical simulation with a two dimensional full-wave model. We run the simulation of whistler emission launched above $\boldsymbol{f_{cp}}$ with various initial WNAs. We analyze the simulation results and summarize our principle conclusions as follows:

1. Characteristic frequencies such as $\boldsymbol{f_{cp}}$, $\boldsymbol{f_{cr}}$, and $\boldsymbol{f_{cut}}$ can redistribute the wave energy of a downward propagating whistler emission in the low-altitude ionosphere. The downward propagating right-hand polarized whistler emission with an intermediate WNA from above $\boldsymbol{f_{cp}}$ splits into two portions at $\boldsymbol{f_{cr}}$. One portion is converted to a right-hand polarized EMIC through linear mode coupling and tunneled below $\boldsymbol{f_{cut}}$. The other portion experiences polarization reversal and reflects upward at $\boldsymbol{f_{cut}}$.
2. The upward propagating left-hand polarized reflected whistler emission splits again at $\boldsymbol{f_{cr}}$. One portion continues as a right-hand polarized whistler after a polarization reversal and propagates above $\boldsymbol{f_{cp}}$. The other portion is converted to a left-hand polarized EMIC through mode conversion and propagates below $\boldsymbol{f_{cp}}$.
3. The efficiency of mode conversion from a downward propagating right-hand polarized whistler to a downward propagating right-hand polarized H^+ band EMIC decreases with its initial WNA. The efficiency decreases from over 80% to almost zero with the initial WNA increased from **15**° to a critical angle **55**°. High efficiency for a small initial WNA explains the propagation features of type C hiss emission observed by Freja and type I hiss emission observed by DEMETER in the high-latitude ionosphere. Moreover, the efficiency to produce left-handed upgoing H^+ band EMIC through mode conversion maximizes at an intermediate initial WNA about **45**°.
4. The downward propagating right-hand polarized whistler emission from above $\boldsymbol{f_{cp}}$ with a large incident WNA (**70**°) reflects at $\boldsymbol{f_{cut}}$ with no significant energy being tunneled down and propagates near $\boldsymbol{f_{cp}}$ in an oscillatory path to the equator. This type of propagation verifies the previously proposed waveguide and explains the characteristics of the types A and F hiss emissions observed by Freja and the type II hiss emission observed by DEMETER in the ionosphere at lower latitude.

Although a smooth plasma density model is adopted in our simulation, complex structures like plasma density troughs with nightside-dayside asymmetry are sometimes observed in both the ionosphere and the plasmasphere (Fu, Tu, Cao et al., 2010; Fu, Tu, Song et al., 2010). Variation of ion composition due to the density troughs can change the local characteristic frequencies such as $\boldsymbol{f_{cr}}$ and $\boldsymbol{f_{cut}}$. Furthermore, the steep density gradients of the plasma density troughs may confine these low-altitude hiss emissions and modify their WNAs. It should be noted that collisions are neglected in our simulation box near the topside ionosphere. However, in the lower region of the ionosphere, the electron-ion, and the neutral collisions become important and may have an impact on the propagation of the low-altitude hiss (Gurevich, 1978; Schunk & Nagy, 2000). The above effects that are not considered in this study may contribute to the mode conversion efficiency and suggest new phenomena of the low-altitude hiss, which needs further investigation with both numerical simulation and satellite observation.

In our study, the upward propagating parallel left-hand polarized H^+ band EMIC wave converted through mode coupling is predicted from simulation cases of both intermediate and large WNA. However, no such cases have been reported yet in observations of low-altitude hiss emission by Freja and DEMETER (Santolík & Parrot, 1998, 1999; Chen et al., 2017; Xia et al., 2019). This is probably due to the sensitive WNA dependence of the mode conversion efficiency. The WNA of hiss emissions observed by Freja and

DEMETER is generally smaller than 15° or larger than 65° (Figure 4c of Santolík & Parrot, 1999; Figures 1c and 1i of Chen et al., 2017; Figure 1c of Xia et al., 2019) while the mode conversion efficiency of a left-hand polarized whistler to a left-hand polarized H^+ band EMIC with a WNA in these ranges is low (~20% or lower). Despite its weak intensity compared with other portions, the energy of the upward propagating left-hand polarized EMIC wave can still be transferred to protons through cyclotron resonant absorption near f_{cp}, which can lead to the heating and energization of protons and contribute to the formation of a proton conics distribution in the high-latitude ionosphere (Chust & Le Que´au, 1996; Le Que´au et al., 1993; Rauch et al., 1993). This phenomenon associated with upward propagating left-handed polarized H^+ band waves needs further observational evidence in the high-latitude ionosphere.

Acknowledgments
The simulation data in this paper can be accessed via the following link http://doi.org/10.5281/zenodo.3614799 link. No observational data are used. X. X. would like to acknowledge the support by China Scholarship Council during his visit to the University of Texas at Dallas. L. C. acknowledges the support of the AFOSR grant of FA9550-16-1-0344. C. Z. acknowledges the support of the National Natural Science Foundation of China (NSFC grants 41574146 and 41774162), the National Key R&D Program of China (grant 2018YFC1503506), the foundation of National Key Laboratory of Electromagnetic Environment (grant 6142403180204), and by Excellent Youth Foundation of Hubei Provincial Natural Science Foundation (grant 2019CFA054).

References

Abel, B., & Thorne, R. M. (1998). Electron scattering loss in Earth's inner magnetosphere: 1. Dominant physical processes. *Journal of Geophysical Research*, *103*, 2385–2396. https://doi.org/10.1029/97JA02919

Bortnik, J., Chen, L., Li, W., Thorne, R. M., & Horne, R. B. (2011). Modeling the evolution of chorus waves into plasmaspheric hiss. *Journal of Geophysical Research*, *116*, A08221. https://doi.org/10.1029/2011JA016499

Bortnik, J., Li, W., Thorne, R. M., Angelopoulos, V., Cully, C., Bonnell, J., et al. (2009). An observation linking the origin of plasmaspheric hiss to discrete chorus emissions. *Science*, *324*(5928), 775–778. https://doi.org/10.1126/science.1171273

Bortnik, J., Thorne, R. M., & Meredith, N. P. (2008). The unexpected origin of plasmaspheric hiss from discrete chorus emissions. *Nature*, *452*(7183), 62–66. https://doi.org/10.1038/nature06741

Budden, K. G. (1985). *The propagation of radio waves, Cambridge Univ*. New York: Press.

Chen, L., Bortnik, J., Li, W., Thorne, R. M., & Horne, R. B. (2012). Modeling the properties of plasmaspheric hiss: 1. Dependence on chorus wave emission. *Journal of Geophysical Research*, *117*, A05201. https://doi.org/10.1029/2011JA017201

Chen, L., Jordanova, V. K., Spasojevic, M., Thorne, R. M., & Horne, R. B. (2014). Electromagnetic ion cyclotron wave modeling during the geospace environment modeling challenge event, J. Geophys. Res. *Space Physics*, *119*, 2963–2977. https://doi.org/10.1002/2013JA019595

Chen, L., Santolík, O., Hajoš, M., Zheng, L., Zhima, Z., Heelis, R., et al. (2017). Source of the low-altitude hiss in the ionosphere. *Geophysical Research Letters*, *44*, 2060–2069. https://doi.org/10.1002/2016GL072181

Chum, J., & Santolík, O. (2005). Propagation of whistler-mode chorus to low altitudes: Divergent ray trajectories and ground accessibility. *Annales de Geophysique*, *23*, 3727–3738. https://doi.org/10.5194/angeo-23-3727-2005

Chust, T., & Le Que´au, D. (1996). Resonant absorption of downward propagating electromagnetic hiss. *Journal of Geophysical Research*, *101*, 10,695–10,710.

Dunckel, N., & Helliwell, R. A. (1969). Whistler-mode emissions on the OGO 1 satellite. *Journal of Geophysical Research*, *74*, 6371–6385. https://doi.org/10.1029/JA074i026p06371

Fu, H. S., Tu, J., Cao, J. B., Song, P., Reinisch, B. W., Gallagher, D. L., & Yang, B. (2010). IMAGE and DMSP observations of a density trough inside the plasmasphere. *Journal of Geophysical Research*, *115*, A07227. https://doi.org/10.1029/2009JA015104

Fu, H. S., Tu, J., Song, P., Cao, J. B., Reinisch, B. W., & Yang, B. (2010). The nightside-to-dayside evolution of the inner magnetosphere: Imager for Magnetopause-to-Aurora Global Exploration Radio Plasma Imager observations. *Journal of Geophysical Research*, *115*, A04213. https://doi.org/10.1029/2009JA014668

Gurevich, A. V. (1978). *Nonlinear phenomena in the ionosphere*. New York: Springer-Verlag.

Helliwell, R. A. (1965). *Whistlers and related ionospheric phenomena*. Stanford, Calif: Stanford Univ. Press.

Hu, Y., & Denton, R. E. (2009). Two-dimensional hybrid code simulation of electromagnetic ion cyclotron waves in a dipole magnetic field. *Journal of Geophysical Research*, *114*, A12217. https://doi.org/10.1029/2009JA014570

Kageyama, A., Sugiyama, T., Watanabe, K., & Sato, T. (2006). A note on the dipole coordinates. *Computational Geosciences*, *32*, 265–269. https://doi.org/10.1016/j.cageo.2005.06.006

Le Que´au, D., Roux, A., Rauch, J. L., Lefeuvre, F., & Bosqued, J. M. (1993). Heating of protons by resonant absorption in a multicomponent plasma, 2, Theoretical model. *Journal of Geophysical Research*, *98*, 13,363–13,375.

Li, W., Chen, L., Bortnik, J., Thorne, R. M., Angelopoulos, V., Kletzing, C. A., et al. (2015). First evidence for chorus at a large geocentric distance as a source of plasmaspheric hiss: Coordinated THEMIS and Van Allen Probes observation. *Geophysical Research Letters*, *42*, 241–248. https://doi.org/10.1002/2014GL062832

Liu, X., Chen, L., Yang, L., Xia, Z., & Malaspina, D. M. (2018). One-dimensional full wave simulation of equatorial magnetosonic wave propagation in an inhomogeneous magnetosphere. *Journal of Geophysical Research: Space Physics*, *123*(1), 587–599. https://doi.org/10.1002/2017JA024336

Lyons, L. R., & Thorne, R. M. (1973). Equilibrium structure of radiation belt electrons. *Journal of Geophysical Research*, *78*, 2142–2149. https://doi.org/10.1029/JA078i013p02142

Means, J. D. (1972). Use of the three-dimensional covariance matrix in analyzing the polarization properties of plane waves. *Journal of Geophysical Research*, *77*, 5551–5559.

Rauch, J. L., Lefeuvre, F., Le Que´au, D. A., Roux, A., Bosqued, J. M., & Berthelier, J. J. (1993). Heating of proton Conics by resonant absorption in a multicomponent plasma, 1, Experimental evidence. *Journal of Geophysical Research*, *98*, 13,347–13,361.

Russell, C. T., Holzer, R. E., & Smith, E. J. (1969). OGO 3 observations of ELF noise in the magnetosphere: 1. Spatial extent and frequency of occurrence. *Journal of Geophysical Research*, *74*, 755–777. https://doi.org/10.1029/JA074i003p00755

Samimi, A., & Simpson, J. J. (2015). An efficient 3-D FDTD model of electromagnetic wave propagation in magnetized plasma. *IEEE Transactions on Antennas and Propagation*, *63*(1), 269–279. https://doi.org/10.1109/TAP.2014.2366203

Santolík, O., Chum, J., Parrot, M., Gurnett, D. A., Pickett, J. S., & Cornilleau-Wehrlin, N. (2006). Propagation of whistler mode chorus to low altitudes: Spacecraft observations of structured ELF hiss. *Journal of Geophysical Research*, *111*, A10208. https://doi.org/10.1029/2005JA011462

Santolík, O., & Parrot, M. (1998). Propagation analysis of electromagnetic waves between the helium and proton gyrofrequencies in the low-altitude auroral zone. *Journal of Geophysical Research*, *103*(A9), 20,469–20,480. https://doi.org/10.1029/98JA01386

Santolík, O., & Parrot, M. (1999). Case studies on the wave propagation and polarization of ELF emissions observed by Freja around the local proton gyrofrequency. *Journal of Geophysical Research*, *104*(A2), 2459–2475. https://doi.org/10.1029/1998JA900045

Santolík, O., & Parrot, M. (2000). Application of wave distribution function methods to an ELF hiss event at high latitudes. *Journal of Geophysical Research*, *105*(A8), 18,885–18,894. https://doi.org/10.1029/2000JA900029

Schunk, R. W., & Nagy, A. F. (2000). *Ionospheres, physics, plasma physics, and chemistry, Cambridge Atmospheric and Space Science Series, Cambridge Univ*. New York: Press.

Stix, T. H. (1992). *Waves in plasmas*. New York: AIP Press.

Streltsov, A. V., Lampe, M., Manheimer, W., Ganguli, G., & Joyce, G. (2006). Whistler propagation in an inhomogeneous plasma. *Journal of Geophysical Research*, *111*, A03216. https://doi.org/10.1029/2005JA011357

Streltsov, A. V., Woodroffe, J. R., & Huba, J. D. (2012). Propagation of whistler mode waves through the ionosphere. *Journal of Geophysical Research*, *117*, A08302. https://doi.org/10.1029/2012JA017886

Taflove, A., & Hagness, S. C. (2005). *Computational electromagnetics: Finite-difference time-domain method*. Norwell, MA, USA: Artech House.

Thorne, R. M., Smith, E. J., Burton, R. K., & Holzer, R. E. (1973). Plasmaspheric hiss. *Journal of Geophysical Research*, *78*, 1581–1596. https://doi.org/10.1029/JA078i010p01581

Xia, Z., Chen, L., Zhima, Z., Santolík, O., Horne, R. B., & Parrot, M. (2019). Statistical characteristics of ionospheric hiss waves. *Journal of Geophysical Research: Space Physics*. https://doi.org/10.1029/2019GL083275

Yee, K. (1966). Numerical solution of initial boundary value problems involving Maxwell's equation in isotropic media. *IEEE Transactions on Antennas and Propagation*, *14*(3), 302–307.

Zhima, Z., Chen, L., Xiong, Y., Cao, J., & Fu, H. (2017). On the origin of ionospheric hiss: A conjugate observation. *Journal of Geophysical Research: Space Physics*, *122*, 11,784–11,793. https://doi.org/10.1002/2017JA024803